



Universiteit
Leiden
The Netherlands

Universal size-dependent nonlinear charge transport in single crystals of the Mott insulator Ca_2RuO_4

Avallone, G.; Fermin, R.; Lahabi, K.; Granata, V.; Fittipaldi, R.; Cirillo, C.; ... ; Aarts, J.

Citation

Avallone, G., Fermin, R., Lahabi, K., Granata, V., Fittipaldi, R., Cirillo, C., ... Aarts, J. (2021). Universal size-dependent nonlinear charge transport in single crystals of the Mott insulator Ca_2RuO_4 . *Npj Quantum Materials*, 6(1). doi:10.1038/s41535-021-00394-7

Version: Publisher's Version

License: [Creative Commons CC BY 4.0 license](#)

Downloaded from: <https://hdl.handle.net/1887/3245509>

Note: To cite this publication please use the final published version (if applicable).

ARTICLE OPEN



Universal size-dependent nonlinear charge transport in single crystals of the Mott insulator Ca_2RuO_4

G. Avallone^{1,2,4}, R. Fermin^{1,4}✉, K. Lahabi¹, V. Granata², R. Fittipaldi³, C. Cirillo³, C. Attanasio², A. Vecchione³ and J. Aarts¹✉

The surprisingly low current density required for inducing the insulator to metal transition has made Ca_2RuO_4 an attractive candidate material for developing Mott-based electronics devices. The mechanism driving the resistive switching, however, remains a controversial topic in the field of strongly correlated electron systems. Here we probe an uncovered region of phase space by studying high-purity Ca_2RuO_4 single crystals, using the sample size as principal tuning parameter. Upon reducing the crystal size, we find a four orders of magnitude increase in the current density required for driving Ca_2RuO_4 out of the insulating state into a non-equilibrium phase which is the precursor to the fully metallic phase. By integrating a microscopic platinum thermometer and performing thermal simulations, we gain insight into the local temperature during simultaneous application of current and establish that the size dependence is not a result of Joule heating. The findings suggest an inhomogeneous current distribution in the nominally homogeneous crystal. Our study calls for a reexamination of the interplay between sample size, charge current, and temperature in driving Ca_2RuO_4 towards the Mott insulator to metal transition.

npj Quantum Materials (2021)6:91 | <https://doi.org/10.1038/s41535-021-00394-7>

INTRODUCTION

Strongly correlated electron systems, and in particular the metallic oxides, have truly marked a paradigm shift in physics, inspiring a decades-long search for exciting quantum materials to explore exotic phenomena, such as high-temperature superconductivity¹, electron hydrodynamics^{2,3}, and holography^{4,5}. A prime example of this, is the family of ruthenates which exhibits a rich and diverse phase diagram that includes Mott insulators^{6,7}, unconventional superconductivity^{8,9}, and magnetism^{10,11}. The $4d$ electron Mott insulator Ca_2RuO_4 ⁶ (hereafter $\text{Ca}214$) has become the subject of intense research in recent years due to its intriguing electrical^{12–24} and magnetic properties^{25,26}. Specifically, at room temperature it undergoes a current-driven insulator to metal transition (IMT) which occurs at unusually low electric (E -)field or current density (J) thresholds (~ 40 V/cm or few A/cm² respectively)^{27,28}. This is in contrast to previous reports on Mott insulators, where the IMT is limited to low temperatures and/or to the application of high E -fields^{29,30}. The capacity to switch between resistive states at room temperature is a desirable property to realize current switchable memories, neuromorphic devices, and next-generation oxide electronics^{31,32}.

The underlying mechanism responsible for such low current densities is still a topic of intense debate. Due to its high resistivity in the insulating state, Joule heating plays a significant role since the IMT can also be thermally driven by heating the crystal above 357 K¹⁸. This has led to ambiguity about the origin of the IMT, and whether it is thermally or electronically driven, as evident by the large number of works discussing local heating^{17,28,33–37}. Specifically, in a recent work, it was found that the IMT is always accompanied by a local temperature increase to the transition temperature³³. Moreover, as a precursor to the metallic phase, a third and non-equilibrium (also called metastable) phase has been detected by X-ray and neutron diffraction experiments, and

additionally with Raman spectroscopy^{14–16}. This non-equilibrium phase seems to be induced by low current densities, but its role in the current-driven IMT remains elusive. Another major hurdle is the pronounced structural transition accompanying the IMT, in which the RuO_2 octahedra are elongated, and the unit cell is transformed from orthorhombic to tetragonal^{13–15,17,27,38,39}. This transition leads to a strong temperature dependence of the unit cell volume ($\sim 1\%$ between 100 K and 400 K), introducing large internal strains in the crystal, often resulting in the formation of cracks or even shattering the crystal upon reentering the insulating phase³⁸.

Although it is much debated whether the IMT is primarily triggered by Joule heating or driven by electronic effects, a parameter that has been left unexplored in this discussion is the size of the samples. Decreasing the size of bulk samples down to μm range gives larger control over current paths in the crystal (due to the uniform rectangular cross section). Furthermore, micro cracks and step-like terraced edges, which occur naturally in mm-sized bulk crystals, are scarce in microscopic samples. Also, since the voltage contacts cover the full side of the microscopic samples, current injection is more homogeneous. This is in contrast with mm-sized crystals where point contacts, and their entailing current crowding effects, are more common. Finally, due to the enhancement of the surface-to-volume ratio and the direct contact with an isothermal substrate, the microscopic samples are expected to be less susceptible to thermal gradients and heating effects.

Here we carry out an extensive size-dependent study using a large number (39) of ultra-pure single crystal samples of $\text{Ca}214$, ranging between the hundreds of nm and the millimeter scale. We examine the role of the current density in inducing the non-equilibrium phase, which we can probe reversibly (i.e., without inducing the IMT and consequently damaging or altering the

¹Huygens-Kamerlingh Onnes Laboratory, Leiden University, P.O. Box 9504, 2300 RA Leiden, The Netherlands. ²Dipartimento di Fisica “E.R. Caianiello”, Università degli Studi di Salerno - Via Giovanni Paolo II, 132 - I-84084 - Fisciano, SA, Italy. ³CNR-SPIN, c/o Università degli Studi di Salerno - Via Giovanni Paolo II, 132 - I-84084 - Fisciano, SA, Italy. ⁴These authors contributed equally: G. Avallone, R. Fermin. ✉email: fermin@physics.leidenuniv.nl; aarts@physics.leidenuniv.nl

crystal). We find a surprising enhancement of the required current density by at least four orders of magnitude upon decreasing the cross section. By integrating a micrometer-sized platinum thermometer, we are able to directly probe the local temperature of the microscopic samples, and demonstrate that the pronounced size dependence is not caused by thermal effects. Our findings call for a careful reexamination of the relevant mechanism behind the non-equilibrium phase and its relation to the IMT in Ca214.

RESULTS

Characterizing microscopic samples

To examine the crossover from large mm-sized bulk behavior to the microscopic one, we have produced samples of varying cross section between 0.5 mm^2 and $0.5 \mu\text{m}^2$. The microscopic samples were fabricated using mechanical exfoliation⁴⁰. This enables us to produce micron-sized “crystal flakes”, which can be lithographically contacted for electrical transport measurements, without compromising the material quality. In addition to the microscopic samples, we have fabricated mm-sized bulk samples that are hand-contacted by the use of silver paint. We employed a focused Ga^+ -ion beam (FIB) as the principal structuring technique throughout this work. This provides us with the means to control the cross section in a systematic manner. Figure 1a, b show

scanning electron microscope and optical microscope images of samples in microscopic and mm-sized ranges respectively.

All measurements are carried out by biasing a current in the ab-plane rather than a voltage, since inducing the metallic state by the application of electric field is more abrupt and therefore the crystals are more likely to break. Furthermore, current density as a function of electric field is hysteretic which complicates the study of size effects carried out here. We have conducted electric field versus current density ($E(J)$ -characteristic) and resistivity measurements as a function of temperature and found that the microscopic samples qualitatively show similar behavior as the mm-sized bulk samples¹⁴. Typical results from microscopic samples are summarized in Fig. 1c, d. It is important to note that, despite several orders of magnitude of size variation, we find the room temperature resistivity of all our samples (microscopic and mm-sized bulk) to be comparable, and in good agreement with the literature values⁶. Curiously, however, the temperature-induced IMT is broadened in microscopic samples with respect to those observed in mm-sized bulk samples (see Fig. 1d). We attribute the broadening of the transition to the small sample thickness since similar effects are observed in thin film samples^{41–44}. We did observe an abrupt change in resistivity upon cooling a relatively thick ($1.5 \mu\text{m}$) microscopic sample through the metal to insulator transition for further discussion on this aspect the reader is referred to the Supplementary Note 2.

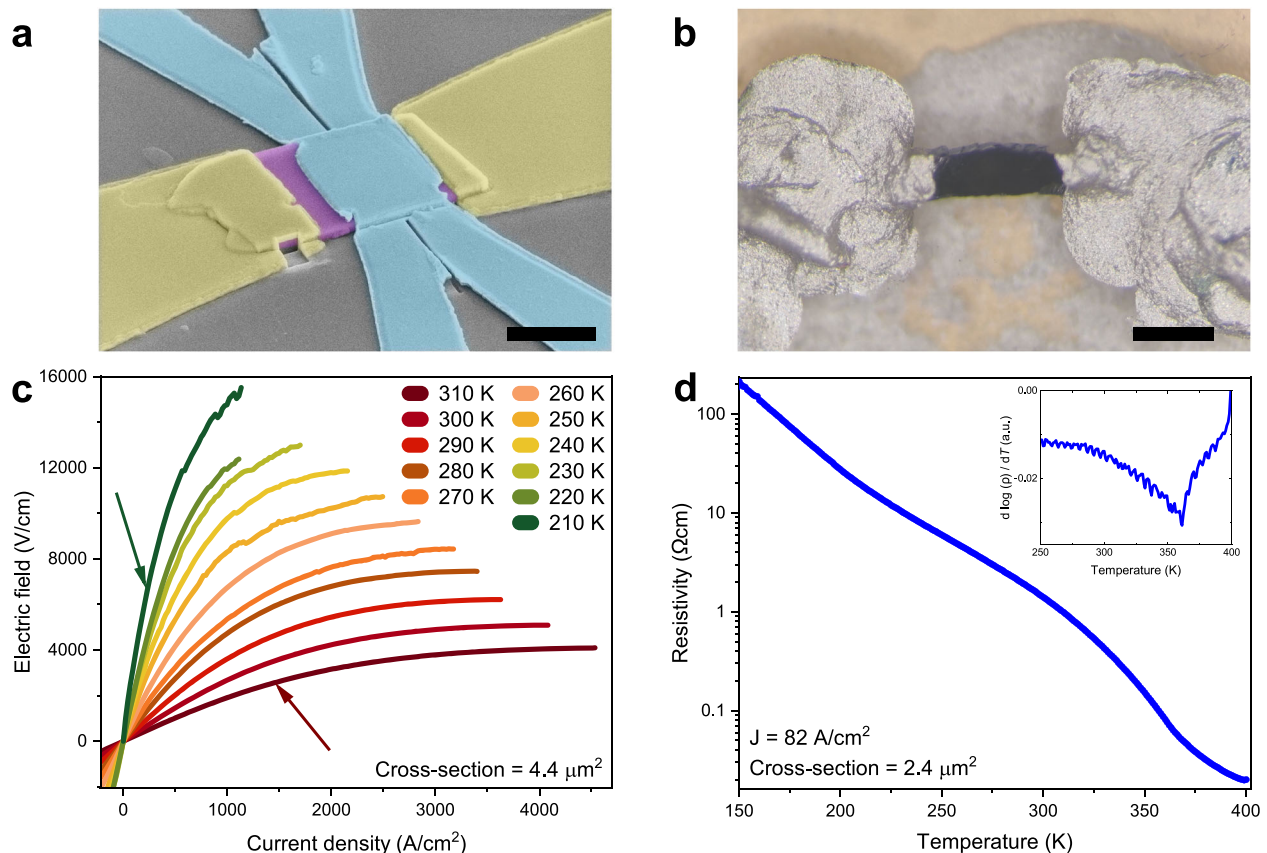


Fig. 1 Transport characteristics of microscopic samples. **a** Displays a false colored scanning electron micrograph of a microscopic sample (in purple) that is contacted by yellow colored Ti/Au contacts. In blue the embedded Pt-thermometer, which can be employed to locally measure the temperature, is shown. The scale bar represents 3 μm . **b** Shows an optical microscope image of an mm-sized sample, where the scale bar measures 500 μm . Panel **c** shows $E(J)$ -characteristics acquired on a microscopic sample at different temperatures. The arrows indicate the current density that would correspond to the Figure of Merit. Note that these curves are obtained below the IMT. The resistivity versus temperature of a typical microscopic sample is shown in panel **d**. In the microscopic size range, we do not observe a sharp temperature-induced IMT, however, as indicated by the inset (the derivative of the curve in the main figure), there is a clear inflection point indicating the thermal transition.

Comparing samples of different cross section

Figure 1c shows $E(J)$ -characteristics obtained on a microscopic sample at different temperatures. These curves qualitatively show similar behavior as the mm-sized bulk samples. However, the current density required for triggering the metastable phase, which is indicated by a negative dE/dJ as a function of J , exceeds the literature values (for mm-sized crystals) by at least four orders of magnitude^{17,27,33}. This is demonstrated in Fig. 2a, where we plot the differential resistivity dE/dJ as a function of J for selected samples. The current density at which dE/dJ begins to decline, corresponding to nonlinear conduction, increases if the sample size is reduced to microscopic scales. In order to compare the nonlinear conduction under applied current between different samples in a systematic manner, we propose a Figure of Merit (FOM) that can be applied to samples of different sizes (see Fig. 2). First, differential resistivity versus current density curves are computed by analytically differentiating the $E(J)$ -characteristics (Fig. 2a). The curves are then normalized with respect to their low current value (i.e., currents for which the resistivity is current independent and conduction is linear). We choose the current density at which the slope of the $E(J)$ -curve has halved as our Figure of Merit, called the 50%-slope current density. The choice for this FOM is suitable since we can compare the size dependence of the $E(J)$ -characteristic in a regime where heating effects play a relatively unimportant role. Furthermore, at the FOM current density, neither the metallic phase nor even the metastable phase is induced in the sample¹⁴. However, we find the shape of the $E(J)$ -curves to be the same between all measured samples. Therefore, the current density required for inducing the metastable phase scales with the FOM current density accordingly, which allows for determining the current density needed to induce the metastable phase. Lastly, the slope of the differential resistivity appears to be maximal at the FOM. Therefore, the choice of this FOM leads to a small uncertainty in the estimated current density, which would not be the case when using the current density at the maximum E -field, for instance.

Figure 2b displays the FOM as a function of the sample cross section for all measured samples. The current density at which

nonlinear conduction sets in, grows monotonically with decreasing sample dimensions and, curiously, the FOM shows a power law dependence on the cross-sectional area. To exclude any potential artifacts associated with sample preparation, we performed a thinning study on three samples over a large size range. We incrementally modify the width and thickness of the same crystal through consecutive FIB structuring steps, and measure the $E(J)$ -characteristic, after each one. Following this procedure, we changed the width of a single microscopic sample in up to seven different thinning steps. Moreover, in an mm-sized bulk sample, we were able to decrease the sample width by a factor 50. Samples on which a thinning experiment was carried out are encircled and highlighted in Fig. 2b by a non-circular symbol and a different color. The FOM as a function of only the width or thickness of the sample (see Supplementary Note 3) reveals the size dependence is not exclusively formed by any of these two parameters but is rather a combination between them, which means that neither of these dimensions is more significant in determining the transport properties of the crystal. The simplest combination of the two parameters is the cross section, which is chosen in Fig. 2b. Supplementary Figure 5 shows the FOM as a function of volume.

Despite the clear trend in Fig. 2b, there is a sample to sample variation that cannot be explained by the uncertainty in the measured crystal dimensions. The deviation from the trend in the mm-sized samples can be explained by irregular current paths in the sample and inconstant cross-sectional area throughout the length of the sample. For the microscopic samples, this does not hold. However, the ratio between width and thickness differs among the samples, and therefore they are expected to respond differently to decreasing dimensions if surface layer effects are important. Furthermore, oxygen relocation can play a role in modifying the crystal structure when passing a current, resulting in a change of transport properties between current cycles. This is consistent with our observations, where, in some cases, the $E(J)$ -characteristic slightly changes after different current or temperature cycles. These arguments can explain the increase in spread observed in Fig. 2b.

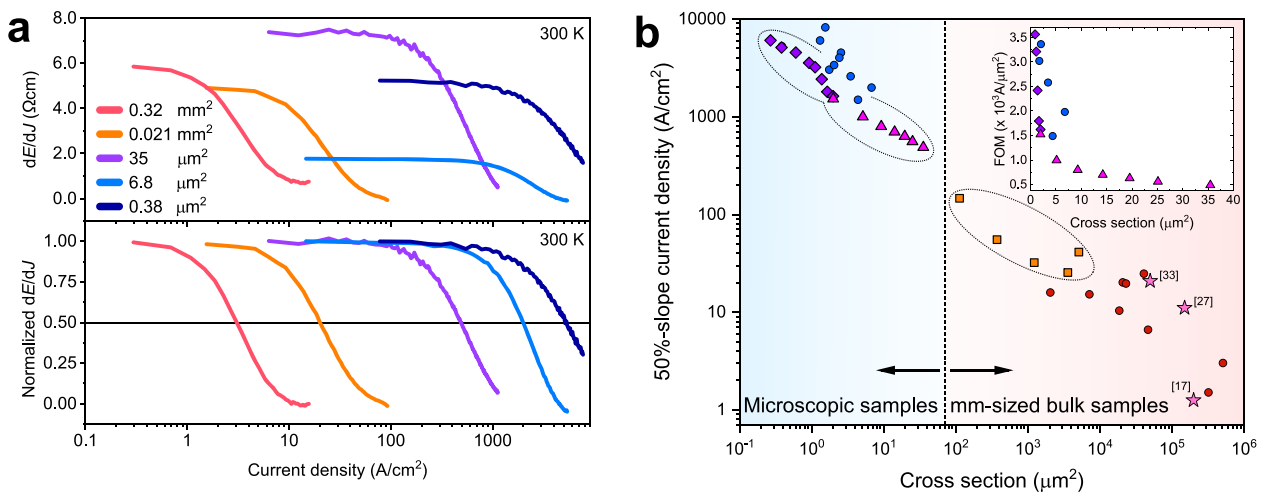


Fig. 2 Size dependence of nonlinear conduction. The top panel of **a** shows the differential resistivity dE/dJ as a function of current density of a few selected samples at room temperature. The legend shows the cross-sectional area of these samples. For all microscopic and mm-sized bulk samples the low current resistivity at room temperature is found to be corresponding to the literature values. In the lower panel of **a**, the differential resistivity of these samples is normalized with respect to the low current resistivity (i.e., where the resistivity is current independent). Even though the $E(J)$ -characteristics of all samples are qualitatively the same, the current density scale at which they exhibit nonlinear conduction differs orders of magnitude. The current density at which the slope of the $E(J)$ -characteristic is halved, is chosen as the Figure of Merit (FOM), which corresponds to the horizontal reference line. **b** Shows the FOM as a function of cross-sectional area for all measured samples at room temperature on a log-log scale. N.B. each circular point corresponds to a single sample. The thinning study samples are depicted with a unique non-circular symbol and a different color. The inset displays the FOM vs sample cross section for selected samples on linear scales. The star symbols correspond to the FOM extracted from literature; the label indicates the reference number.

The role of temperature

All the experiments reported previously, where the temperature is locally measured in Ca214, are carried out on mm-sized bulk samples using optical techniques, as local contact thermometry is experimentally difficult to realize at these dimensions. Microscopic samples do not have this limit and enable contact thermometry to give insight into the local sample temperature. To implement this, we carefully designed and fabricated a platinum thermometer on top of selected microscopic samples (see Fig. 1a). Since platinum has a distinctly linear temperature dependence, we are able to accurately measure the temperature of the microscopic samples, while simultaneously driving a current using an independent bias (see Supplementary Note 1 for details).

In order to make plausible that the temperature difference between the Pt and the sample is negligible and to investigate the likelihood of potential temperature gradients in the sample, we have performed thermal simulations accompanying the thermometry results. Here we solved for a steady-state temperature, under the assumption that heat is generated uniformly in the crystal flake while the substrate temperature remains constant 50 μm away from the sample. The full technical details of these simulations can be found in Supplementary Note 6.

Figure 3a displays the platinum temperature obtained on the sample shown in Fig. 1a (orange curve) together with the simulation results as a function of current density. The measured

temperature is exceeding the expected averaged Pt temperature (purple curve) for high currents. This can be caused by the absence of heat transfer barriers between the simulated elements, whereas in experiments these can be expected. The purple curve can therefore be considered as a lower bound of the expected Pt temperature. Nevertheless, the simulated average sample (green curve) and Pt temperature (purple curve), show correspondence to a high degree. We have also examined temperature gradients in the sample and found temperature differences to be limited to 3 K in the sample (see Fig. 3c and Supplementary Note 6). Furthermore, we evaluate the maximum temperature within the simulated flake geometry (blue curve) and compare it to the simulated average Pt temperature. We find these to differ < 2 K at the FOM current density. Therefore, we consider our Pt thermometry technique suited for acquiring the average sample temperature at the FOM. At the FOM current density, the locally measured temperature increase is found to be < 10 K. Therefore, we conclude that Joule heating is non-zero but similar to mm-sized bulk samples³³.

The measurement of the local temperature enables us to calculate what the $E(J)$ -characteristic would look like based on heating effects only. For the resistivity versus temperature measurement on this sample, we compute the dE/dJ from our $E(J)$ -characteristics for low currents (i.e., where the resistivity ρ is

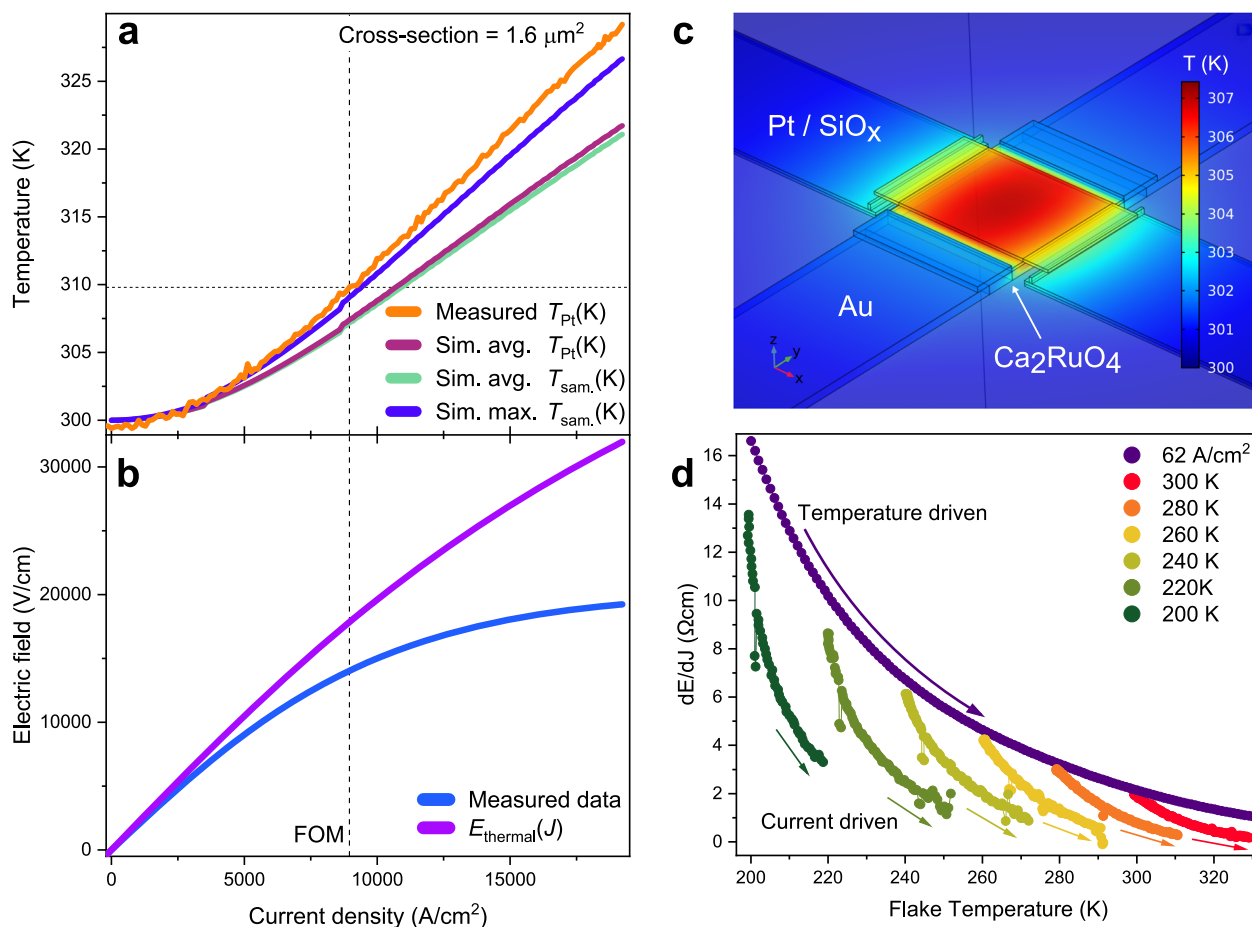


Fig. 3 The role of temperature in microscopic samples. **a** Displays the local measured Pt temperature and multiple simulated temperatures as a function of the applied J . The data is acquired on the sample depicted in Fig. 1a. The substrate temperature is 300 K. **b** Shows the electric field acquired simultaneously with the temperature measurement. The measured data is compared to E_{thermal} (i.e., the calculated electric field on basis of Joule heating only). The vertical reference line indicates the FOM. The local temperature increase at the FOM is below 10 K. A simulated temperature heatmap of the sample at the FOM current density is shown in **c**. **d** Displays the differential resistivity as a function of the flake temperature. Either the background temperature or the current density is changed. At all current densities, the nonlinear conduction is stronger than heating effects can provide.

current independent):

$$\rho(T) = \frac{dE}{dJ}(T, J \approx 0) \quad (1)$$

Since the temperature is homogeneous up to a variation of 3 K over the entire sample, we can use the locally measured temperature as a function of current density to find the dE/dJ as a function of heating effects:

$$\frac{dE_{\text{thermal}}}{dJ}(J) = \frac{dE}{dJ}(T(J), J \approx 0) = \rho(T(J)) \quad (2)$$

Integrating the Eq. (2), we can reconstruct the $E(J)$ -characteristic that would have been measured if Joule heating was the only mechanism causing the nonlinear conduction. We set the integration constant by requiring zero electric field for zero current density ($E(0) = 0$; see Supplementary Note 5 for more details):

$$E_{\text{thermal}}(J) = \int \frac{dE_{\text{thermal}}}{dJ}(J) dJ \quad (3)$$

We denote this reconstructed function as $E_{\text{thermal}}(J)$ and plot it alongside the measured data in Fig. 3b. Even at low current densities, the actual measured data shows stronger nonlinear conduction than $E_{\text{thermal}}(J)$, indicating that current-driven effects are significant in the microscopic samples for all applied current densities probed in this study.

Alternatively, the differential resistivity as a function of local sample temperature is plotted in Fig. 3d. The purple curve describes the resistivity as a function of temperature with a constant current density (62 A/cm²). Alongside, we plot the differential resistivity as a function of increasing bias current, while maintaining a constant substrate temperature. Evidently, the slope decrease of $E(J)$ -characteristic, caused by the application of current, is not primarily driven by Joule heating.

We conclude based on our thermometry experiments that the size dependence presented in Fig. 2b cannot be explained by Joule heating. Furthermore, we find that a current-driven mechanism is present parallel to Joule heating in the non-equilibrium phase.

DISCUSSION

Before discussing the possible origin of the observed size dependence, we consider the following notes. Firstly, there seems to be no intrinsic length scale found in our measurements. This can be seen from the absence of a specific cross section where the FOM changes discontinuously. Secondly, we can exclude the effects of microcracks since the size dependence continues even in the microscopic regime where micro cracks are not present. By inspecting the samples with a scanning electron microscope, we could confirm that no micro cracks were induced by measuring the $E(J)$ -characteristic. Thirdly, the observation of a current-driven mechanism parallel to Joule heating, as observed here, was recently also reported by Jenni et al.³⁴. Lastly, we note that our findings are consistent with the reports on epitaxially grown thin films of Ca214, where the current density required to induce the IMT was also found to be many orders of magnitude higher than in bulk literature values⁴¹.

The emergence of the metallic phase was recently attributed by Terasaki et al.³⁶ to energy flow, as opposed to charge transport. In this study, the energy flow corresponds to the dissipated power (product of current and voltage IV), in contrast, here it is more insightful to describe the product of electric field and current density EJ (power dissipation density), enabling the comparison of samples of different length scales. Since microscopic samples show a four order of magnitude increase in current density at which we observe nonlinear transport, we find that the power dissipation density is eight orders of magnitude larger in

microscopic samples than in mm-sized bulk samples (see Supplementary Figure 8a). It is therefore unlikely that the energy flux through the crystal is responsible for observed size dependence.

Alternatively, the size dependence might be explained by strain, induced through coupling to the substrate. In the zero-current limit, however, the substrate does not exercise any strain on the crystal, as we will discuss below. The room temperature resistivity of Ca214 is strongly dependent on strain and the IMT can be induced by applying 0.5 GPa of pressure^{13,23,24}. By using ultra-low currents (\sim nA), we have confirmed that the insulating-state resistivity of the microscopic samples matches that of their mm-sized counterparts, signaling the absence of strain. Moreover, in a previous work on the isostructural unconventional superconductor Sr₂RuO₄, we have prepared microscopic samples using equal methods and substrates⁴⁵. These samples retained bulk properties to sizes below 200 nm, whereas, like Ca214, its transport properties are heavily dependent on strain^{46–48}. Therefore we conclude that our microscopic samples do not experience strain at zero current bias. In simultaneous transport and X-ray diffraction measurements, it has been shown that at the FOM current density, there is no detectable change of the lattice parameters¹⁴. Combined with the absence of strain at zero current bias, this leads to the conclusion that our samples do not experience any strain at the FOM, regardless of their size. Thus, we do not regard strain as a plausible explanation for the observed size dependence.

Near the IMT, and independent of whether that is induced by current or temperature, the arguments supporting the absence of strain no longer hold, as the lattice constants significantly alter^{14,15}. Although we are far below the IMT in our current-driven experiments, we pass the IMT in the temperature sweep, presented in Fig. 1d. Strain-related effects could be responsible for the observed broadening of the transition. Moreover, a broadened transition is commonly observed in thin films, where strain induced by the substrate is expected to be an influential parameter^{41–43}.

Finally, an inhomogeneous distribution of current throughout the cross-sectional area could potentially explain the size dependence found here. Since the current density is calculated by dividing the applied current by the entire cross section, the apparent current density in mm-sized bulk samples might be lower than the actual current density that is physically relevant. Due to their size and geometry, however, in the microscopic samples, the apparent and actual current densities can be more similar.

Metallic filament formation, which is known to occur in Mott insulators⁴⁹, may induce such highly inhomogeneous current distributions. Contrarily, for Ca214, Zhang et al.¹⁷ inspected phase separation using scanning near field optical microscopy (SNOM) and found a ripple pattern at the phase boundary between the insulating and metallic states. Although the resolution of the SNOM technique might be insufficient to rule out sub 100 nm channel formation, it is difficult to reconcile the striped pattern found in SNOM with filament formation at present.

Furthermore, Zhang et al. find that the metallic phase nucleates at the top of the sample, and its depth increases when traversing a phase boundary in the phase-separated state. This could suggest an inhomogeneous distribution of current throughout the cross-sectional area, that is high at the edges of the crystal and decreases towards the center of the bulk. Since the microscopic crystals have a larger surface-to-volume ratio, the edges are relatively more dominant. If the current density gradually increases below the current-carrying surface, this proposed mechanism will not feature any length scale at which a discontinuous change is expected in the FOM, which is compatible with our findings. In Supplementary Note S7, a minimal toy model describing the inhomogeneous current density

is presented. This model can reproduce the power law dependence observed in Fig. 2b.

In conclusion, we have performed a detailed study on size-dependent electrical properties of the Mott insulator Ca_2RuO_4 . We find a surprising relation between crystal size and the current density at which nonlinear conduction occurs, which increases four orders of magnitude when the sample size is reduced from 0.5 mm^2 to $0.5 \text{ }\mu\text{m}^2$. We have strong indications that the observed size dependence is not caused by Joule heating, using a local Pt-thermometer fabricated on top of selected microscopic samples. Our findings indicate an intrinsically inhomogeneous current density distribution in single crystals of Ca_2RuO_4 . This calls for a reexamination of the relevant role of current in the metastable phase and its possible relation to the IMT. As an outlook, the combination of microscopic samples with a well-controlled current path, and local platinum temperature probes, provides a state-of-the-art approach to study the interplay between thermal and electronic effects, which can be used to study the IMT in Mott insulators.

METHODS

Crystal growth

Bulk single crystals of Ca_{214} were grown by a flux feeding floating zone technique with Ru self-flux using a commercial image furnace equipped with double elliptical mirrors described elsewhere^{50,51}. Several techniques, including X-ray diffraction, energy dispersive spectroscopy, and polarized light optical microscopy analysis, have been used to fully characterize the structure, quality, and purity of the crystals.

Sample fabrication and transport experiments

The microscopic samples were fabricated by the use of mechanical exfoliation on highly resistive SrTiO_3 or sapphire substrates. The flake samples are significantly thicker than monolayers. Therefore, random strain patterns, wrinkles, and folds associated with the thin film limit are absent. Due to the natural shape of the crystal flakes, the produced samples are suited best for passing current in the ab-plane. Therefore all experiments are carried out in this configuration.

Considerable effort was put into the fabrication of the electrical connections on the samples to reduce the contact resistance that possibly becomes an extrinsic origin for nonlinear conduction due to local Joule heating. To perform electrical transport measurements, the samples obtained by the exfoliation process were contacted by means of an electron beam lithography step followed by a Ti/Au sputtering deposition and a lift-off procedure. When necessary, we used electron beam induced deposition to provide an electrical reinforcement of the contacts by locally depositing an additional layer of tungsten-carbide on them. On the mm-sized samples, we found a resistive background in the $E(J)$ -characteristics, from which we extracted the contact resistance to be $< 10 \text{ }\Omega$, which is significantly smaller than the sample resistance, supporting the use of a two-probe measurement. Some microscopic samples were contacted in a 4-probe geometry. Using these samples, we could confirm that the contact resistance is negligible in comparison to the sample resistance. In addition to the microscopic samples, we have fabricated conventionally mm-sized bulk samples that are contacted by hand using silver paint (Agar Scientific G3691).

The electrical transport measurements were carried out by applying a current using a Keithley 6221 current source. The voltage drop over the sample was measured using a Keithley 2182a nanovolt meter.

Microscopic thermometry and FIB-processing

In a second step of electron beam lithography, the Pt-thermometer was added to selected samples. The Pt-circuit is electrically isolated by a thin layer of sputter-deposited SiO_x ($\sim 100 \text{ nm}$). This ensures that the Pt-thermometer and sample form two decoupled electrical systems. The resistance between the Pt-circuit and the Ca_{214} sample was found to be over $1 \text{ G}\Omega$ and the $E(J)$ -characteristic measured before and after the application of the Pt-thermometer was found unaffected, as demonstrated in Supplementary Note 1.

We used the FIB technique to modify both the sample width and thickness enabling the full control of sample dimensions and geometry

over a large crystal size range (see Supplementary Note 4). After fabrication, we have confirmed by scanning electron microscope inspection that the microscopic samples lack any micro cracks.

DATA AVAILABILITY

The data that support the findings of this study are available from the corresponding author upon reasonable request.

Received: 29 January 2021; Accepted: 16 October 2021;

Published online: 10 November 2021

REFERENCES

- Keimer, B., Kivelson, S. A., Norman, M. R., Uchida, S. & Zaanen, J. From quantum matter to high-temperature superconductivity in copper oxides. *Nature* **518**, 179–186 (2015).
- Moll, P. J. W., Kushwaha, P., Nandi, N., Schmidt, B. & Mackenzie, A. P. Evidence for hydrodynamic electron flow in PdCoO_2 . *Science* **351**, 1061–1064 (2016).
- Sulpizio, J. A. et al. Visualizing Poiseuille flow of hydrodynamic electrons. *Nature* **576**, 75–79 (2019).
- Maldacena, J. M. The large N limit of superconformal field theories and supergravity. *Int. J. Theor. Phys.* **38**, 1113–1133 (1999).
- Hartnoll, S. A., Lucas, A. & Sachdev, S. Holographic quantum matter. Preprint at <http://arxiv.org/abs/1612.07324> (2016).
- Nakatsuji, S., Ikeda, S.-i & Maeno, Y. Ca_2RuO_4 : new Mott insulators of layered ruthenate. *J. Phys. Soc. Jpn* **66**, 1868–1871 (1997).
- Zhu, M. et al. Colossal magnetoresistance in a Mott insulator via magnetic field-driven insulator-metal transition. *Phys. Rev. Lett.* **116**, 216401 (2016).
- Maeno, Y., Kittaka, S., Nomura, T., Yonezawa, S. & Ishida, K. Evaluation of spin-triplet superconductivity in Sr_2RuO_4 . *J. Phys. Soc. Jpn* **81**, 011009 (2012).
- Leggett, A. J. & Liu, Y. Symmetry properties of superconducting order parameter in Sr_2RuO_4 : A brief review. *J. Supercond. Nov. Magn.* **34**, 1647–1673 (2020).
- Cao, G., McCall, S., Crow, J. E. & Guertin, R. P. Observation of a metallic anti-ferromagnetic phase and metal to nonmetal transition in $\text{Ca}_3\text{Ru}_2\text{O}_7$. *Phys. Rev. Lett.* **78**, 1751–1754 (1997).
- Grigera, S. A. et al. Magnetic field-tuned quantum criticality in the metallic ruthenate $\text{Sr}_3\text{Ru}_2\text{O}_7$. *Science* **294**, 329–332 (2001).
- Alireza, P. L. et al. Evidence of superconductivity on the border of quasi-2D ferromagnetism in Ca_2RuO_4 at high pressure. *J. Condens. Matter Phys.* **22**, 052202 (2010).
- Nakamura, F. et al. From Mott insulator to ferromagnetic metal: A pressure study of Ca_2RuO_4 . *Phys. Rev. B* **65**, 220402 (2002).
- Cirillo, C. et al. Emergence of a metallic metastable phase induced by electrical current in Ca_2RuO_4 . *Phys. Rev. B* **100**, 235142 (2019).
- Bertinshaw, J. et al. Unique crystal structure of Ca_2RuO_4 in the current stabilized semimetallic State. *Phys. Rev. Lett.* **123**, 137204 (2019).
- Fürsich, K. et al. Raman scattering from current-stabilized nonequilibrium phases in Ca_2RuO_4 . *Phys. Rev. B* **100**, 081101 (2019).
- Zhang, J. et al. Nano-resolved current-induced insulator-metal transition in the Mott insulator Ca_2RuO_4 . *Phys. Rev. X* **9**, 011032 (2019).
- Alexander, C. S. et al. Destruction of the Mott insulating ground state of Ca_2RuO_4 by a structural transition. *Phys. Rev. B* **60**, R8422–R8425 (1999).
- Nakatsuji, S., Ando, T., Mao, Z. & Maeno, Y. Metal-insulator transition in $\text{Ca}_{x-2}\text{Sr}_x\text{RuO}_4$. *Phys. B Condens. Matter* **259–261**, 949–950 (1999).
- Nakatsuji, S. & Maeno, Y. Quasi-two-dimensional Mott transition system $\text{Ca}_{x-2}\text{Sr}_x\text{RuO}_4$. *Phys. Rev. Lett.* **84**, 2666–2669 (2000).
- Nakatsuji, S. & Maeno, Y. Synthesis and single-crystal growth of $\text{Ca}_{x-2}\text{Sr}_x\text{RuO}_4$. *J. Solid State Chem.* **156**, 26 – 31 (2001).
- Sutter, D. et al. Orbitally selective breakdown of Fermi liquid quasiparticles in $\text{Ca}_{1.8}\text{Sr}_{0.2}\text{RuO}_4$. *Phys. Rev. B* **99**, 121115 (2019).
- Steffens, P. et al. High-pressure diffraction studies on Ca_2RuO_4 . *Phys. Rev. B* **72**, 094104 (2005).
- Nakamura, F. Pressure-induced Mott transition and related novel quantum phenomena in Ca_2RuO_4 . *J. Phys. Soc. Jpn* **76**, 96–99 (2007).
- Braden, M., André, G., Nakatsuji, S. & Maeno, Y. Crystal and magnetic structure of Ca_2RuO_4 magnetoelastic coupling and the metal-insulator transition. *Phys. Rev. B* **58**, 847–861 (1998).
- Zegkinoglou, I. et al. Orbital ordering transition in Ca_2RuO_4 observed with resonant X-ray diffraction. *Phys. Rev. Lett.* **95**, 136401 (2005).
- Nakamura, F. et al. Electric-field-induced metal maintained by current of the Mott insulator Ca_2RuO_4 . *Sci. Rep.* **3**, 2536 (2013).

28. Okazaki, R. et al. Current-induced gap suppression in the mott insulator Ca_2RuO_4 . *J. Phys. Soc. Jpn* **82**, 103702 (2013).
29. Taguchi, Y., Matsumoto, T. & Tokura, Y. Dielectric breakdown of one-dimensional Mott insulators Sr_2CuO_3 and SrCuO_2 . *Phys. Rev. B* **62**, 7015–7018 (2000).
30. Kanki, T., Kawatani, K., Takami, H. & Tanaka, H. Direct observation of giant metallic domain evolution driven by electric bias in VO_2 thin films on $\text{TiO}_2(001)$ substrate. *Appl. Phys. Lett.* **101**, 243118 (2012).
31. Yang, Z., Ko, C. & Ramanathan, S. Oxide electronics utilizing ultrafast metal-insulator transitions. *Annu. Rev. Mater. Res.* **41**, 337–367 (2011).
32. Stoliar, P. et al. A leaky-integrate-and-fire neuron analog realized with a Mott insulator. *Adv. Funct. Mater.* **27**, 1604740 (2017).
33. Mattoni, G., Yonezawa, S., Nakamura, F. & Maeno, Y. Role of local temperature in the current-driven metal-insulator transition of Ca_2RuO_4 . *Phys. Rev. Mater.* **4**, 114414 (2020).
34. Jenni, K. et al. Evidence for current-induced phase coexistence in Ca_2RuO_4 and its influence on magnetic order. *Phys. Rev. Mater.* **4**, 085001 (2020).
35. Okazaki, R. et al. Current-induced giant lattice deformation in the Mott insulator Ca_2RuO_4 . *J. Phys. Soc. Jpn* **89**, 044710 (2020).
36. Terasaki, I. et al. Non-equilibrium steady state in the Mott insulator Ca_2RuO_4 . *J. Phys. Soc. Jpn* **89**, 093707 (2020).
37. Chiriacò, G. & Millis, A. J. Polarity dependent heating at the phase interface in metal-insulator transitions. *Phys. Rev. B* **102**, 085116 (2020).
38. Friedt, O. et al. Structural and magnetic aspects of the metal-insulator transition in Ca_2RuO_4 . *Phys. Rev. B* **63**, 174432 (2001).
39. Gorelov, E. et al. Nature of the Mott transition in Ca_2RuO_4 . *Phys. Rev. Lett.* **104**, 226401 (2010).
40. Huang, Y. et al. Reliable exfoliation of large-area high-quality flakes of graphene and other two-dimensional materials. *ACS Nano* **9**, 10612–10620 (2015).
41. Tsurumaki-Fukuchi, A. et al. Stable and tunable current-induced phase transition in epitaxial thin films of Ca_2RuO_4 . *ACS Appl. Mater. Interfaces* **12**, 28368–28374 (2020).
42. Miao, L. et al. Itinerant ferromagnetism and geometrically suppressed metal-insulator transition in epitaxial thin films of Ca_2RuO_4 . *Appl. Phys. Lett.* **100**, 052401 (2012).
43. Wang, X., Xin, Y., Stampe, P. A., Kennedy, R. J. & Zheng, J. P. Epitaxial thin film growth of $\text{Ca}_2\text{RuO}_{4+\delta}$ by pulsed laser deposition. *Appl. Phys. Lett.* **85**, 6146–6148 (2004).
44. Dietl, C. et al. Tailoring the electronic properties of Ca_2RuO_4 via epitaxial strain. *Appl. Phys. Lett.* **112**, 031902 (2018).
45. Yasui, Y. et al. Spontaneous emergence of Josephson junctions in homogeneous rings of single-crystal Sr_2RuO_4 . *npj Quant. Mater.* **5**, 21 (2020).
46. Grinenko, V. et al. Split superconducting and time-reversal symmetry-breaking transitions in Sr_2RuO_4 under stress. *Nat. Phys.* **17**, 748–754 (2021).
47. Barber, M. E., Gibbs, A. S., Maeno, Y., Mackenzie, A. P. & Hicks, C. W. Resistivity in the vicinity of a van Hove singularity: Sr_2RuO_4 under uniaxial pressure. *Phys. Rev. Lett.* **120**, 076602 (2018).
48. Steppke, A. et al. Strong peak in T_c of Sr_2RuO_4 under uniaxial pressure. *Science* **355**, eaaf9398 (2017).
49. Lange, M. et al. Optical imaging of strain-mediated phase coexistence during electrothermal switching in a Mott insulator. Preprint at <https://arxiv.org/abs/2009.12536> (2020).
50. Fukazawa, H., Nakatsuji, S. & Maeno, Y. Intrinsic properties of the Mott insulator $\text{Ca}_2\text{RuO}_{4+\delta}$ ($\delta = 0$) studied with single crystals. *Phys. B Condens. Matter* **281–282**, 613–614 (2000).
51. Granata, V. et al. Crystal growth of the Ca_2RuO_4 -Ru metal system by the floating-zone technique. *J. Alloy. Compd* **832**, 154890 (2020).

ACKNOWLEDGEMENTS

This work was supported by the Dutch Research Council (NWO) as part of the Frontiers of Nanoscience (NanoFront) program, and through NWO Projectruimte grant 680.91.128. This work benefited from access to the Netherlands Centre for Electron Nanoscopy (NeCEN) at Leiden University. The authors want to thank Jan Zaanen for discussing the results in an early stage of the work and Norman Blümel for additional sample characterization.

AUTHOR CONTRIBUTIONS

V.G., R.F., and A.V. grew the crystals and characterized them for purity. G.A., R.F., and K.L. prepared the microscopic samples and performed the measurements. All authors contributed to writing the manuscript. G.A. and R.F. are considered co-first author.

COMPETING INTERESTS

The authors declare no competing interests.

ADDITIONAL INFORMATION

Supplementary information The online version contains supplementary material available at <https://doi.org/10.1038/s41535-021-00394-7>.

Correspondence and requests for materials should be addressed to R. Fermin or J. Aarts.

Reprints and permission information is available at <http://www.nature.com/reprints>

Publisher's note Springer Nature remains neutral with regard to jurisdictional claims in published maps and institutional affiliations.



Open Access This article is licensed under a Creative Commons Attribution 4.0 International License, which permits use, sharing, adaptation, distribution and reproduction in any medium or format, as long as you give appropriate credit to the original author(s) and the source, provide a link to the Creative Commons license, and indicate if changes were made. The images or other third party material in this article are included in the article's Creative Commons license, unless indicated otherwise in a credit line to the material. If material is not included in the article's Creative Commons license and your intended use is not permitted by statutory regulation or exceeds the permitted use, you will need to obtain permission directly from the copyright holder. To view a copy of this license, visit <http://creativecommons.org/licenses/by/4.0/>.

© The Author(s) 2021